Exceptional strength-ductility synergy of additively manufactured CoCrNi medium-entropy alloy achieved by lattice defects in heterogeneous microstructures

Jianying Wang[1], Jianpeng Zou[1], Hailin Yang[1,*], Lijun Zhang[1], Zhilin Liu[2], Xixi Dong[3], Shouxun Ji[3]

1. State Key Laboratory of Powder Metallurgy, Central South University, Changsha 410083, China
2. Light Alloy Research Institute, College of Mechanical and Electrical Engineering, Central South University, Changsha, 410083, China
3. Brunel Centre for Advanced Solidification Technology (BCAST), Brunel University London, Uxbridge, Middlesex, UB8 3PH, United Kingdom
* Corresponding author, email: y-hailin@csu.edu.cn

Abstract: The selective laser melting (SLM) with subsequent cold rolling and annealing are used to produce high-density lattice defects and grain refinement in the CoCrNi medium-entropy alloys (MEAs). The superior comprehensive mechanical properties have been achieved in the as-SLMed CoCrNi alloy after rolling and annealing. The as-SLMed alloys delivered the yield strength of 693.4 MPa, the ultimate tensile strength of 912.7 MPa and the fracture strain of 54.4%. After rolling with 70% reduction in thickness and annealing at 700 ºC for 2 h. the yield strength, ultimate tensile strength and fracture strain reached 1161.6 MPa, 1390.8 MPa and 31.5%, respectively. The exceptional strength-ductility synergy is mainly attributed to the refined hierarchical microstructures with coarse grains at a level of 30 μm and ultrafine grains at a level of 1 μm, and the heritage of dislocation-formed sub-grains and other lattice defects. This investigation demonstrates that the SLM with subsequent rolling and annealing are beneficial to fabricate high strength and ductile MEAs with single face-centred cubic (fcc) structure.

Keywords: Medium-entropy alloys, Selective laser melting, Strength-ductility synergy, Defects, Microstructure

1. Introduction

Medium/High-entropy alloys (MEAs/HEAs) are highly considered as potential candidates to replace conventional metallic materials owing to their superior mechanical, physical and chemical properties [1–6]. Among the multi-principal element alloys, CoCrNi MEAs have increasingly attracted much attention due to the unprecedent properties, especially the exceptional ductility, fracture toughness at room and cryogenic temperatures because of the plastic deformation modes, i.e., dissociated $\{111\}1/6\langle 112\rangle$ partial dislocation in the early stage under tension and the subsequent unusual activation of nano-twins and transformation-induced plasticity (TRIP) effect [7–14]. In particular, the formation of deformed twins resulted from the low stacking fault energy (SFE) in {111} planes are one of the primary deformation mechanisms for the CoCrNi alloys at low temperatures [8,9]. Meanwhile, the CoCrNi alloys can form stable and thick passive film on the surface and thus present excellent corrosion resistance [15]. However, CoCrNi alloys with single face-centred cubic (fcc) crystal structure can offer superior ductility and fracture toughness, but the yield strength is usually lower than 400 MPa, which is insufficient for many engineering applications. The essential technical development is carrying out to conquer such challenge [5,8,16–19].

Generally, tailoring lattice defects (i.e. dislocation and nano-twins) and introducing fine grains are practically achievable to improve the mechanical properties of metallic alloys [20–24]. It was reported that the stacking fault energy (SFE) in CoCrNi alloys is estimated to be 22 mJ/m^2 at room temperature, which is 25% lower than that in CrMnFeCoNi HEAs [8,9,16]. The most commonly observed lattice defects are dislocations, SFs, and annealing (or deformation) twins. These defects tend to be readily formed during rolling, recrystallization and/or partial recrystallization or mechanical deformation [6,7,12–14,16–18]. In addition to the strengthening and hardening originated from the capability of SFs and nanotwins to accommodate dislocations, the SFs and nanotwins can also serve as a continuous source of ductility by providing pathways for the gliding or cross-slipping of dislocations. Meanwhile, grain refinement is one of the most effective ways to strengthen HEAs/MEAs due to the fact that ultrafine grained/nanocrystalline metals are usually much stronger than their coarse-grained counterparts [20–26]. For CoCrFeMnNi alloys, when the grain size is reduced from 155 to 4.5 μm by cold rolling, the yield strength can be dramatically increased from 170 to 360 MPa [20]. Similarly, for the CoCrNi alloys fabricated by arc melting and high-pressure torsion (HPT), the refined microstructure with a grain size of 200 nm can significantly improve the yield strength [24]. Apart from plastic deformation, cooling rates during solidification also play a critical role in grain refinement. Compared with the conventional casting method, spark plasma sintering (SPS) can induce the fine-grained structure by consolidating mixed and/or

pre-alloyed powders at a high cooling rate (normally > 100 ºC/min) [5,18,27,28]. For the SPSed CoCrNi alloys, the average grain size of 4.11 μm delivers relatively high yield strength of 652 MPa [27]. Moreover, through architecting ultrafine grains together with the high density of lattice defects, the SPSed CoCrNi alloys can provide the ultimate tensile strength of 1.4 GPa and the elongation of 7.0% [28]. However, SPS method cannot be widely used for industrial applications due to the size limit.

Selective laser melting (SLM) is a laser-based additive manufacturing technique to develop high-performance and complex structural materials at a high cooling rate up to 10^5–10^6 ºC/s [29–31]. The SLM process is an emerging practice suitable for building metallic materials such as Al-based alloys [30,31], Ti-based alloys [32,33], Fe-based alloys (steels) [34,35], Ni-based alloys [36,37], and HEAs/MEAs [38–41]. The solidification process in the micro-molten pool occurs at a very high cooling rate, which greatly refines the microstructure and thus improves the corresponding mechanical properties. The fine Mg_2Si eutectic phase in SLMed Al-Mg-Si alloys [30,31], ultrafine lamellar (α+β) structures in SLMed Ti alloys [32,33] and fine cellular martensite structures in SLMed steels [33,34] have been found to be able to deliver superior mechanical properties. Also, the hierarchical microstructure being composed of dislocations-formed cellular structures and low-angle grain boundaries (LAGBs) within the complex columnar grains can offer a good yield strength (630～650 MPa) for SLMed CoCrNi alloys [40,41]. Although the clusters of equiaxed sub-grains separated by dislocation walls can promote relatively good dislocation strengthening in CoCrNi alloys, the coarse grains separated by high-angle grain boundaries (HAGBs) in CoCrNi alloys caused by a major epitaxial grain growth due to the large temperature gradients and cooling rates, and thus weaken the grain boundary strengthening. As a result, the mechanical properties of SLMed CoCrNi alloys can be further improved by refining the coarse grains and/or sub-grains.

Cold rolling, one of the plastic deformation techniques, is well known for preparing bulk metallic materials with fine-grained structure and high tensile strength. The microstructure and mechanical properties of cold-rolled SLMed Al, stainless steel and Ni-based superalloys have been intensively investigated [42–44]. Ma et al. [42] found that the refined grains (～2.4 μm) and high-density $Al_3(Sc,Zr)$ particles in the SLMed Al-Mg-Sc-Zr alloys with 86% reduction thickness delivered high yield strength of 573 MPa. Zhang et al. [43] found that the rolling force has an important influence on the microstructure evolution of the cold-rolled Inconel 718 alloys. The more uniformly distributed refined grains, high tensile strength and hardness have been achieved in the alloys with increasing rolling force. Regrettably, little research has been done to analyse the influence of cold rolling on the microstructure and mechanical properties of SLMed CoCrNi alloys. On the one hand, the subsequent rolling process is likely to refine

the coarser hierarchical microstructure that contains dislocation-formed sub-grains in the SLMed CoCrNi alloy, which enhances grain boundary strengthening and dislocation strengthening effects. On the other hand, considering the characteristics of low SFE of CoCrNi alloy, the various kinds of lattice defects (i.e. SFs and nanotwins) induced by the subsequent annealing treatment reduce the free pathways for mobile dislocations and improve mechanical properties further. Therefore, introducing refined grain structure and tailoring crystalline defects through subsequent cold rolling and annealing might be an effective way to achieve excellent comprehensive mechanical properties in the SLMed CoCrNi-based alloy. Although subsequent cold rolling process may weaken the advantage of SLM method, the SLM plus rolling is the first effective attempt to achieve superior mechanical properties of CoCrNi alloys.

Therefore, in this study, it is aimed to explore the capability of introducing different lattice defects into the refined hierarchical microstructure of SLMed CoCrNi alloys along with cold deformation and subsequent annealing. The manufacturing process was optimised with the microstructure to achieve excellent mechanical properties in CoCrNi alloys. The discussion focuses on the effects of hierarchical microstructures on the mechanical properties of SLMed CoCrNi alloys and the dominant mechanisms responsible for strengthening.

2. Experimental section

2.1 Powder and materials fabrication

Pre-alloyed CrCoNi powders with a particle size distribution of 15～53 μm were used in this study. **Fig. 1** shows the powder morphologies, XRD spectra and elemental distribution mappings, confirming the powder are homogeneous and have good sphericity. The signal peaks standing for fcc phase were observed in the pre-alloyed powder. Additionally, EDS mapping confirmed there was no evident elemental segregation within CrCoNi pre-alloyed powders.

The SLM process was conducted using a FS271M (Farsoon, Inc, China) selective laser melting system with the following processing parameters: laser beam diameter of 90 μm, laser power of 400 W, scan speed of 600 mm/s, hatch spacing of 0.12 mm and layer thickness of 0.04 mm. The samples were built layer-by-layer on a substrate plate of 45# carbon steel, which was grit-blasted with alumina prior to installation. The laser scanning was carried out with a 67º rotating scanning layer-by-layer. The SLMed alloys were then cut off from the substrate by electrical discharge machining (EDM). A number of 10 mm thick strips were sliced as the sample under as-SLMed condition. Inductively coupled plasma atomic emission spectrometry (ICAP 7000 Series) was applied to characterize chemical composition of the as-SLMed alloy, as shown in **Table 1**. Subsequently, the sliced samples were rolled by 70% reduction in thickness at room

temperature to form samples under as-rolled condition. Then annealing was applied at 700 ºC for 2 h. Such process was denoted as the RA treatment throughout the present work. The samples were successively ground with 400-, 800-, 1000-, 1500- and 2000-grit SiC abrasive paper, followed by polishing in the 1 μm-sized diamond agent to reach the high-quality surface condition for further characterization.

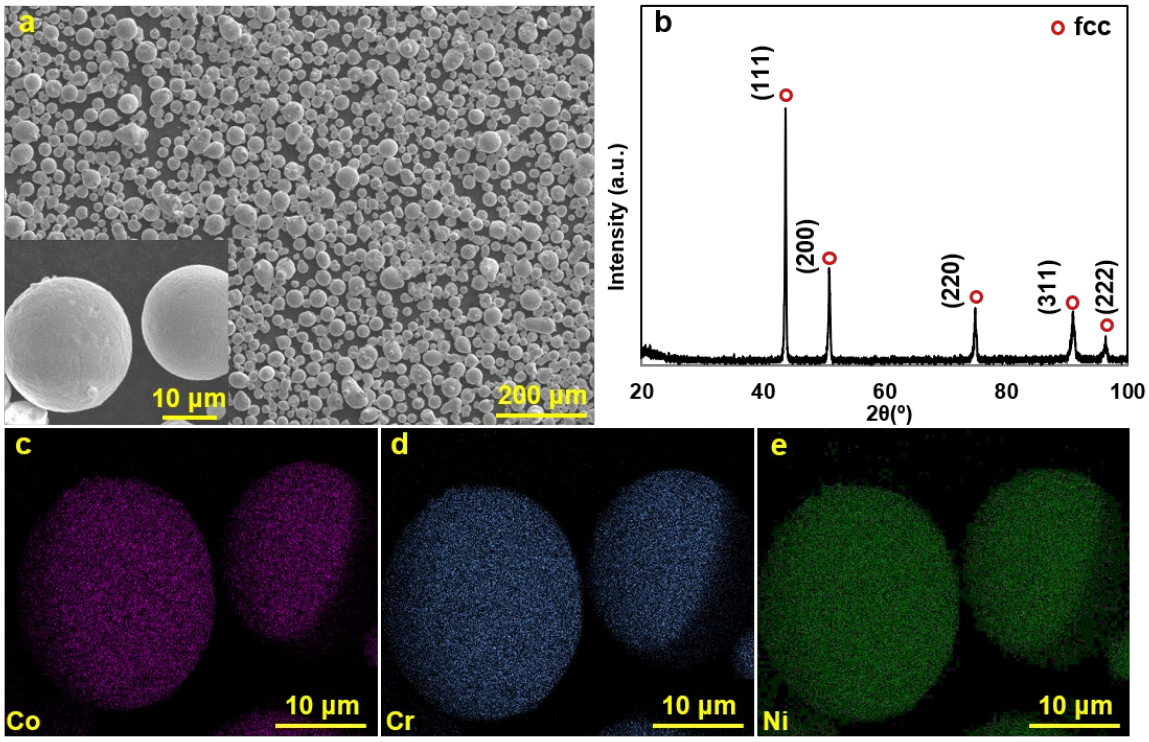

Figure 1. Characterization of pre-alloyed CoCrNi MEA powder; (a) Powder particle morphology; (b) XRD spectra; (c)-(e) EDS mapping for elemental distribution.

Table 1. Chemical Compositions of the CoCrNi as-SLMed alloy (wt.%).

Element	Co	Cr	Ni	Fe	C	O	N	P	S
wt.%	34.9	30.4	34.5	0.063	0.0036	0.0015	0.0021	0.0012	0.00034

2.2 Microstructural characterization

The phase constituent and crystal structure of the CoCrNi alloy under different conditions were examined using X-ray diffraction technique with Cu Ka radiation (XRD, Rigaku). Microstructural features of the alloy were characterized using electron microscopes. Scanning electron microscope (SEM), backscattered electron microscope (BSE) and electron backscattered diffraction (EBSD) orientation mappings were assembled in a FIB Helios NanoLab G3 UC system. Meanwhile, it is also equipped with a Hikari camera and the TSL OIM data analysis software for EBSD. Before EBSD and XRD examination, the samples were

finished by polishing with 40 nm colloidal silica suspension. Before SEM/BSE observation, the samples were polished and etched for 1～4 min in the solution containing 5 g of $CuCl_2$ in 100 ml of HCl and 100 ml of ethanol. Furthermore, the transmission electron microscope (TEM; Titan G2 60-300) was used for detailed microstructure examination. The TEM samples were prepared using the precision ion polishing system (PIPS) at a voltage of 5 kV/2 kV and at an incident angle of 3º ~ 7º.

2.3 Mechanical property evaluation

The bulk density of the samples was measured through the Archimedes method (ASTM, B962-13). Dog-bone-shaped tensile samples were cut by EDM from the printed samples. Both sides of the samples were carefully ground to a 2000 grit finish using SiC papers. The uniaxial tensile tests were performed using a material testing system (MTS Alliance RT30) at room temperature (~25 $^{\circ}$C) with an engineering strain rate of 1×10^{-3} s^{-1}. Micro-hardness was measured by a micro-Vickers hardness tester with a load of 300 g for 10 s (ASTM E 384-08). All the reported data are based on the average value of at least 5 measurements.

3. Results

The engineering tensile stress-strain curves of the SLMed CoCrNi alloys without and with RA treatment are shown in **Fig. 2a**. It is seen that the yield strength was 693.4 MPa, the ultimate tensile strength (UTS) was 912.7 MPa, the fracture strain was 54.4%, and the Vickers hardness was 260.2 Hv under as-SLMed condition. Aadditionally, the relative density of CoCrNi MEA is about 99.6%. After RA treatment, the alloy exhibited a striking improvement in the mechanical performance, at which the yield strength was 1161.6 MPa, the UTS was 1390.8 MPa, the fracture strain was 31.5% and the Vickers hardness was 403.5 Hv. Apparently, an excellent combination of strength and ductility have been achieved. To understand the mechanical properties offered by CoCrNi alloys, **Fig. 2b** shows a comparison of tensile strength of CoCrNi alloys fabricated by different techniques including MA (mechanical alloying) + SPS, casting, SLM in both other literatures and this study [8,16,18,28,27,40,41]. Obviously, the CoCrNi alloys fabricated by SLM in this study provide good combination of strength and ductility. Furher, **Fig. 2c** shows a comparison of tensile strength between the SLMed CoCrNi alloys with RA treatment and CoCrNi alloys fabricated by casting/HPT/SPS with subsequent plastic defornation, and Mo(Ti,Al) doped CoCrNi alloys [14,24,28,45,46]. Similarly, the SLMed CoCrNi alloys with RA treatment provide superior combination of mechanical properties.

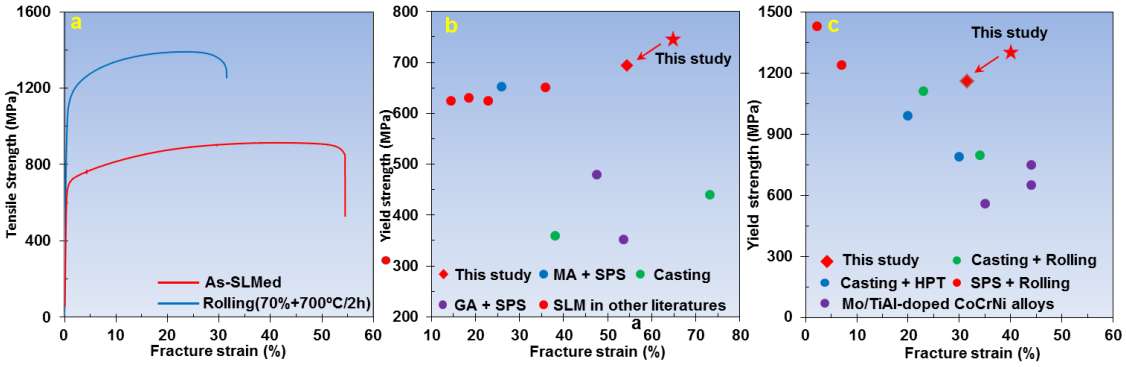

Figure 2. Engineering tensile stress–strain curves of SLMed CoCrNi alloys without and with the 70% reduction in thickness and annealing at 700 ºC for 2 h (RA treatment); (b) Comparison of tensile strength of CoCrNi alloys fabricated by different techniques without subsequent deformation and heat-treatment, including MA + SPS, casting, SLM in other literatures and in this study [8,16,18,28,27,40,41]; (c) Comparison of tensile properties of the as-SLMed CoCrNi alloys with RA treatment obtained from this study and CoCrNi alloys fabricated by casting + rolling, casting + HPT, SPS + Rolling, and Mo/(Ti,Al)-doped CoCrNi alloys [14,24,28,45,46].

The detailed microstructures along the horizontal direction in SLMed CoCrNi alloys are shown in **Fig. 3**. It can be seen that irregular pores were hardly observed from top view, and the thickness of scanning layer in microstructure was about 120 μm, which was consistent with the value pre-set in the machine (**Fig. 3a**). The microstructure acquired under backscattering mode (**Fig. 3b**) identified the formation of hierarchical microstructure. Relatively coarse grains showed the mixture of columnar and equiaxed sub-grains. The sizes of columnar sub-grains were from dozens to hundreds of microns in length and at a level of 300～400 nm in width, while the mean cell size of equiaxed sub-grains was measured to be 0.86 μm (**Figs. 3c&3d**). Additionally, a heat-affected zone (HAZ) can be observed in **Fig. 3e**. Columnar sub-grains were observed nucleating on the melt bottom that consisted of prism-like sub-grains (**Fig. 3f**).

Furthermore, the detailed microstructures along the horizontal direction in the alloys with RA treament are shown in **Fig. 4**. The typical characteristics of SLMed microstructures disappeared and some partially-recrystallized grains were observed. The metallographic features on the cross-sections exhibited heterogeneous distribution of grain sizes (**Fig. 4a**). Clearly, the average grain size of the alloy with RA treatment was much reduced in comparasion with that in its counterpart under SLMed condition. Fine annealing twins with the width of 50-200 nm were also observed after annealing due to the treatment at a low temperature with a short time, as indicated by the yellow arrows in **Fig. 4b**. Particularly, the refined hierarchical microstructures, consisting of the mixture of refined columnar and equiaxed sub-grains, were observed in **Fig. 4c&4d**. Obviously, the width of columnar sub-

grains was significantly decreased after severe rolling, which was about 20 nm (**Fig. 4e**). Interestingly, the annealing twins also occurred in sub-grains. Similarly, the mean cell sizes of equiaxed sub-grains also decreased (**Fig. 4f**).

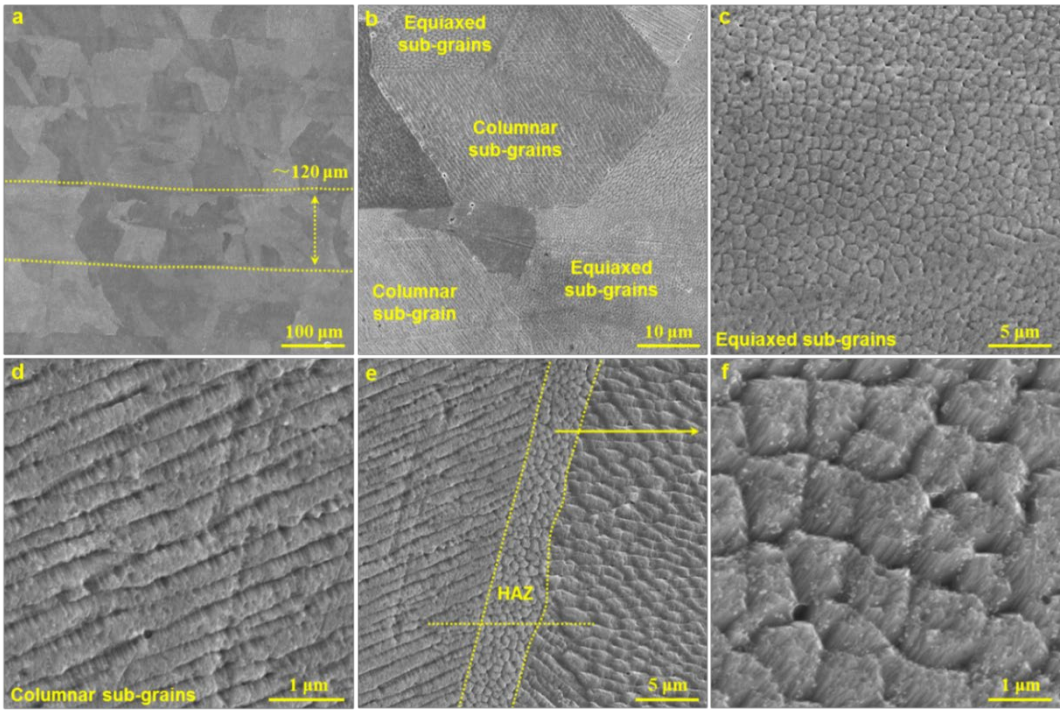

Figure 3. SEM/BSE images showing the microstructure of SLMed CoCrNi alloys; (a) the overall microstructure; (b) the hierarchical microstructure consisted of columnar and equiaxed sub-grains; (c) the detailed microstructure of equiaxed sub-grains; (d) the detailed microstructure of columnar sub-grains; (e) a heat-affected zone (HAZ); and (f) prism-like sub-grains.

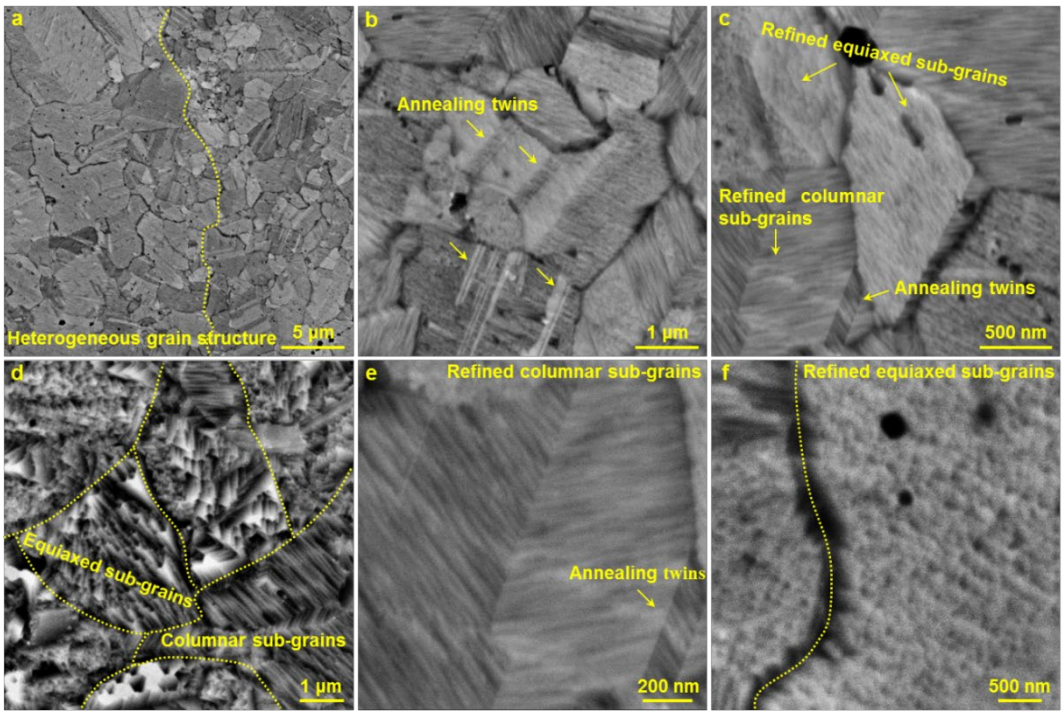

Figure 4. SEM/BSE images showing the microstructure features of SLMed CoCrNi alloys with RA treatment: (a) the overall microstructure; (b) the refined grain structure with annealing twins at nana-sizes; (c) the refined hierarchical microstructure composed of refined columnar and equiaxed sub-grains; (d) the detailed microstructure showing refined hierarchical microstructure after deep inch; (e) the detailed microstructure of refined columnar sub-grains; (f) the detailed microstructure of equiaxed sub-grains. The yellow arrows indicate the formation of annealing twins.

XRD spectra in **Fig. 5** identified the existence of only single fcc phase in the alloys under two conditions. A strong growth texture of ⟨100⟩ was observed at the distinctive {200} peak in the cubic specimens, in contrast to that of raw powder. To clarify, {200} is equivalent to {100} orientation due to multiplicity and extinction in the XRD phase identification process of disordered solid solution fcc metals. However, a growth texture of ⟨100⟩ was weakened in the alloy with RA treatment.

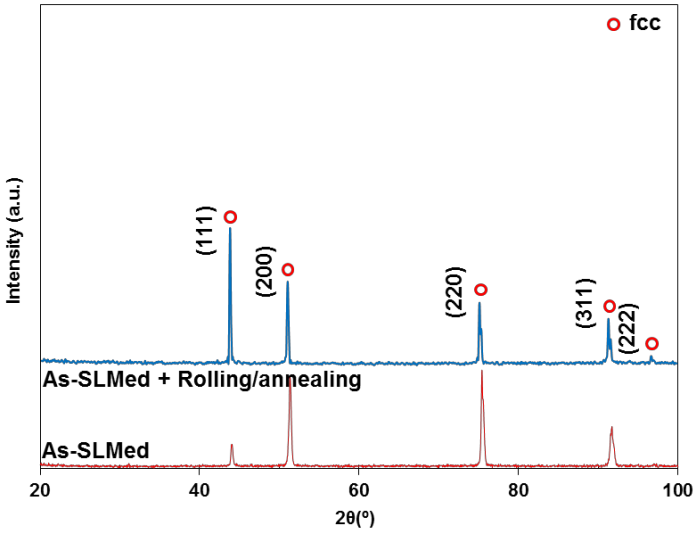

Figure 5. XRD spectra of SLMed CoCrNi alloys without and with RA treatment.

Inverse Pole Figure (IPF) map, Image Quality (IQ), Kernel Average Misorientation (KAM) map of SLMed CoCrNi alloys without and with RA treatment are shown in **Fig. 6** accordingly, and the corresponding data for EBSD testing are summarized in Table 2. As indicated in **Fig. 6a**, the scanning tracks were obviously in line with the scanning direction between the two continuous layers of 67°. Meanwhile, the scanning track consisted of columnar grains, while the boundary of the scanning track consisted of equiaxed grains owing to the Gaussian distribution of the laser energy when scanning the powder bed [47]. The rapid moving of laser beam weakened the temperature gradient in the scanning track. The cooling rate in the middle of the scanning track was the highest compared to that of the surrounding regions and gradually decreased towards the boundary. The average grain size was 47.83 μm. The distributions of misorientation angles map in **Fig. 6b** indicates that the fractions of high-angle grain boundary (HAGB, $\geqslant 15^{o}$) and low-angle grain boundary (LAGB, $<15^{o}$) were 67.4% and 32.6%,

respectively. IPF map in **Fig. 6d** shows a refined grain structure of the alloy with RA treatment having an average size of 5.08 μm. The detailed IPF in **Fig. 6e** and IQ map in **Fig. 6f** indicate the obvious existence of heterogeneous grain structures in the alloy after partial recrystallization. The resultant heterogeneous grain structures contained two types of grains with obviously different length scales and sizes: The coarse grains (> 4 μm) constituted an area fraction of ~43.1%, and the relative fine grains (< 4 μm) comprised an area fraction of 56.9%. Meanwhile, the distribution of misorientation angle map in **Fig. 6f** indicates that the relative higher fractions of low-angle grain boundary are 48.6% with RA treatment. Additionally, the KAM images of SLMed CoCrNi alloys without and with RA treatment are shown in **Fig. 6c&6g**, respectively. The average KAM value of the CoCrNi alloy treated by rolling was 0.908, which was high due to the accumulation of strain energy inside the alloy and the multiplication of dislocations. The variations in average KAM qualitatively reflected the degree of plastic deformation or defect density [48]. Additional stress was introduced into the boundaries of adjacent grains to guarantee strain compatibility during plastic deformation, which increased the density of geometrically necessary dislocation (GND) [49]. According to Equation (1), the KAM map was used to calculate GND by combining local strain [50]:

$$\rho_{GND} = 2\vartheta/(\mu b) \quad (1)$$

where ϑ is the average value of KAM, μ is the step size during EBSD measurement, and b is the Burger vector (0.253 nm [6]). Correspondingly, the ρ_{GND} of SLMed CoCrNi alloys without and with RA treatment was calculated to be ~ 5.42 × 10^{15} m^{-2}, and ~ 1.44 × 10^{16} m^{-2}, respectively. The high density of GNDs would contribute to high strength.

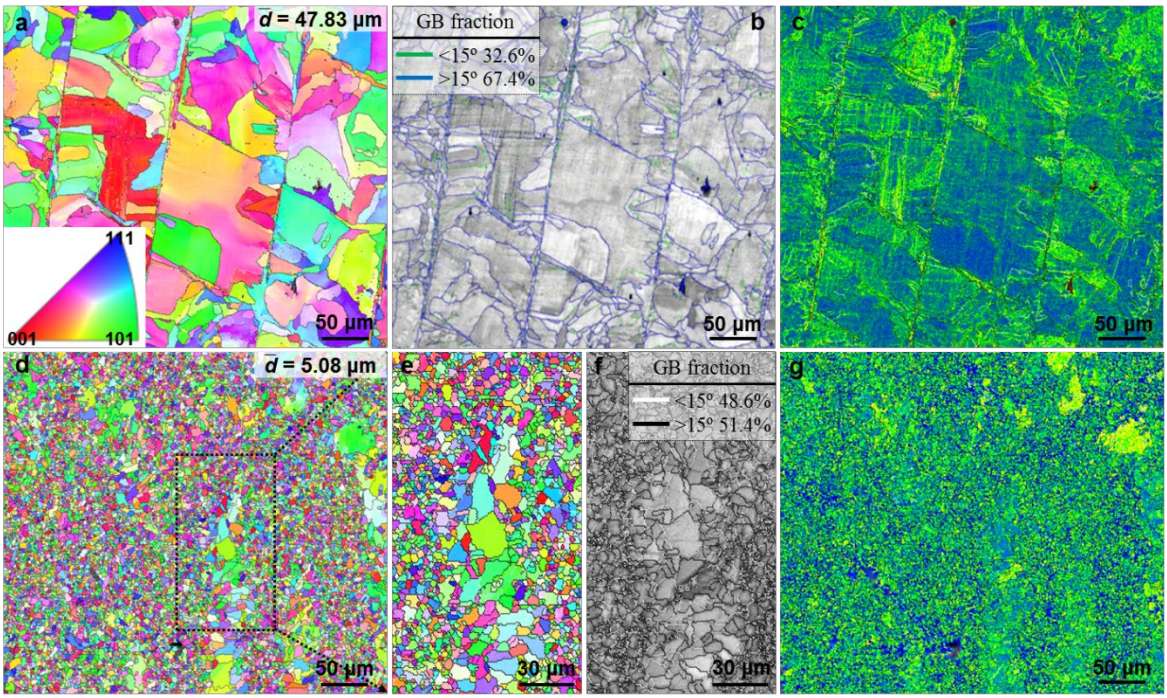

Figure 6. (a) Inverse Pole Figure (IPF) map, (b) Image Quality (IQ) map, (c) Kernel Average Misorientation (KAM) map of SLMed CoCrNi alloys; (d) and (e) detailed IPF map, (f) IQ map, and (g) KAM map of SLMed CoCrNi alloys with RA treatment.

Table 2. The grain size, the step size selected in EBSD testing, length of the Burgers vector, KAM value and ρ_{GND} determined for SLMed CoCrNi alloys without and with RA treatment.

Conditions	Grain size	Step size	|b|	KAM value	ρ_{GND}
As-SLMed	47.83 μm	1.20 μm	0.258 nm	0.839	5.42×10^{15} m^{-2}
RA treatment	5.08 μm	0.50 μm	0.258 nm	0.908	1.44×10^{16} m^{-2}

4. Discussion

4.1 Structure-Property relationship in the SLMed CoCrNi alloys with RA treatment

Like CoCrNi alloys fabricated by other methods, such as casting and SPS, the corresponding strengthening contributions of SLMed CoCrNi alloys mainly depend on grain boundary strengthening and dislocation strengthening since there is no precipitation strengthening and very limited solid solution strengthening. As shown in **Fig. 3** and **Fig. 6a**, the microstructure of the SLMed CoCrNi alloys mainly contains coarse grains with an average grain size of 47.83 μm. Previous studies have shown that the average grain sizes of as-cast CoCrNi alloy and SPSed CoCrNi alloy are 111.00 μm and 20.80 μm, respectively [5,24]. Thus, the contribution of grain boundary strengthening in this study is higher than that of the CoCrNi alloys fabricated by casting, while lower than that of the CoCrNi alloys prepared by SPS. However, the formation of unique nano-scale high-density dislocation-formed sub grains in the SLMed CoCrNi alloys (due to instantaneous temperature drop in the SLM process) possesses outstanding dislocation strengthening [40,41]. Thus, the yield strength of as-cast and SPSed CoCrNi alloys normally lower than 400 MPa, while the SLMed CoCrNi alloys exhibit relatively high yield strength of 693.4 MPa. Conventionally, cold rolling is an effective way to refine the grains and increase the yield strength of as-cast and SPSed CoCrNi alloys [14,28,45,46], the fine grains, high density GNDs coupled with other lattice defects (SFs, deformation twins and so on) induced by severe deformation and the formation of twins after annealing deliver an excellent combination of mechanical properties. Compared with CoCrNi alloys fabricated by cast/SPS with subsequent rolling, the rolling process not only increases the density of GNDs that distributed at the boundaries of adjacent grains of SLMed CoCrNi alloys to ensure strain compatibility during plastic deformation (as shown in **Fig. 6** and **Table. 2**). It is interestingly noted that the microstructure with RA treatment showed obvious heritability from the inherited characteristics of nano-cellular in the matrix. Correspondingly, irregular sub-grains consisted of dislocations can be shown in TEM bright-field (BF) image (**Fig. 7a**) and

STEM image (**Fig. 7b**). Meanwhile, the refined columnar sub-grains with 20-30 nm thickness were detected in TEM BF-image of **Fig. 7c**. Since the dense GNDs would thicken dislocation walls and progressively penetrated into dislocation network, which could act as grain boundaries of adjacent columnar sub-grains [51]. The dislocation walls could be also referred to LAGBs of columnar sub-grains, as indicated in **Fig. 7d**. Additionally, HAADF-STEM image and the elemental mapping of equiaxed and columnar sub-grains are shown in **Fig. 8**. Obviously, all the elements are dispersed uniformly in the SLMed alloys with RA treatment. Thus, like the SLMed Al, stainless steel, and Ni-based superalloys with rolling process [42–44], the microstructure of SLMed CoCrNi alloys can be further refined by cold rolling and the columnar dendrites of SLMed alloys normally changed to finer equiaxed grains, which could result in excellent grain refinement. Although the macro-cellular in the as-SLMed microstructures have been completely destroyed by the severe deformation from rolling, the dislocation-formed sub-grains inside the primary phases could be observed in the samples with RA treatment. This is believed to be significantly beneficial for strengthening the alloy.

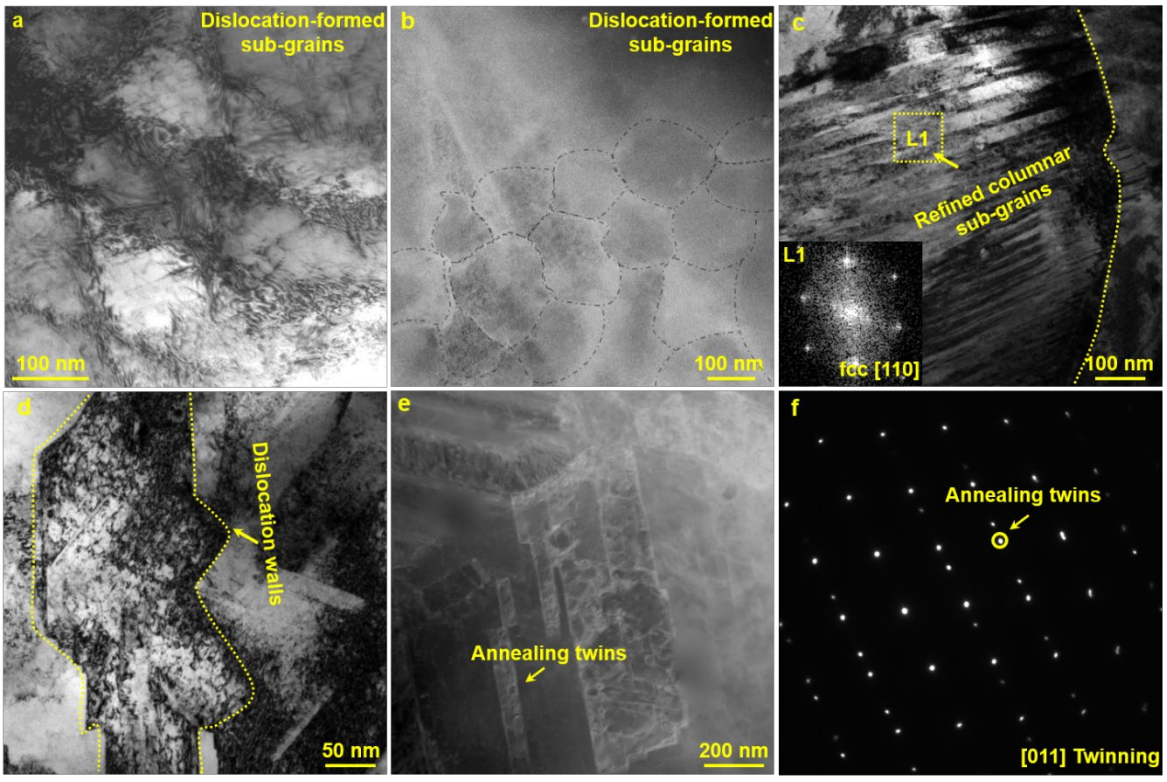

Figure 7. TEM micrographs showing the microstructure of SLMed CoCrNi alloys with RA treatment: (a) TEM image and (b) STEM image of a high-density dislocation-formed equiaxed sub-grains; (c) TEM image of the refined columnar sub-grains; (d) dislocation structure of dislocation walls; (e) STEM and (f) SAED pattern showing the formation of annealing twins with nano-sizes.

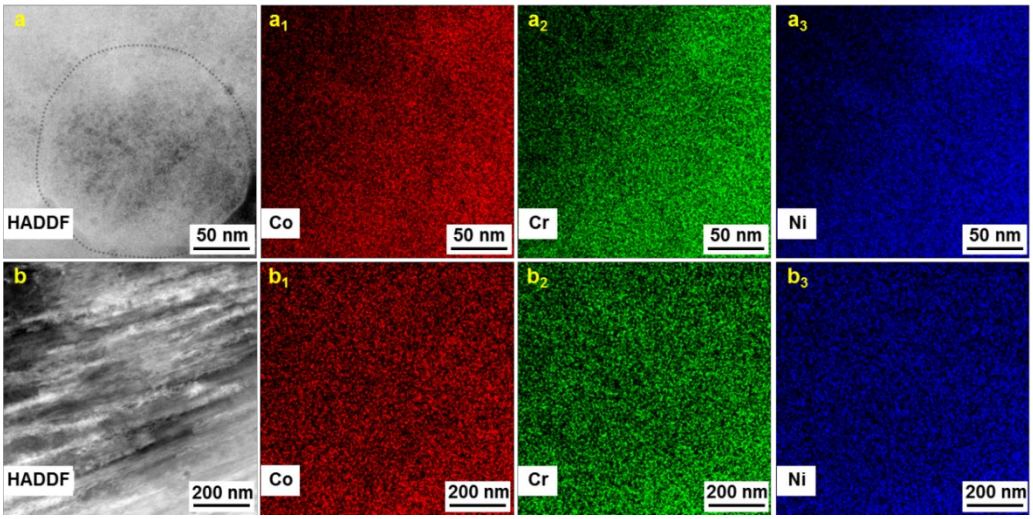

Figure 8. The corresponding EDS mapping of equiaxed sub-grains (a, a_1-a_3) including elements (a_1) Co; (a_2) Cr; (a_3) Ni; and columnar sub-grains (b, b_1-b_3) including elements (b_1) Co; (b_2) Cr; (b_3) Ni.

4.2 Contribution of various strengthening mechanisms

The results showed that the SLMed CoCrNi alloy with RA treatment exhibits the yield strength of 1161.6 MPa, UTS of 1390.8 MPa and fracture strain of 31.5%. As aforementioned, the significant improvement in strength mainly originates from the refined hierarchical microstructures that consisted of the heterogeneous fine grain structure (5.08 μm) and the high-density refined dislocations-formed sub-grains. Since there is no precipitation strengthening and limited solid solution strengthening in the alloy, the high strength is mainly attributed to the synergistic contribution from multiple strengthening mechanisms, including the intrinsic friction stress σ_0, fine grain strengthening (σ_g), and dislocation strengthening (σ_{dis}). Therefore, the contribution of main mechanisms responsible for strengthening of the alloy can be expressed as:

$$\sigma_y = \sigma_0 + \sigma_g + \sigma_{dis} \quad (2)$$

where σ_0 is a constant (218 MPa for CoCrNi alloy [24]). The part of strengthening effects by grain refinement (σ_g) can be calculated via the Hall-Petch equation [52]:

$$\sigma_g = Kd^{-0.5} \quad (3)$$

where K is a constant (265 MPa·μm$^{1/2}$ for CoCrNi alloy [24]). As for the average grain size d in the hierarchical structure, the grain boundary strengthening is referred to the dislocation movement blocked by lattice misfit and intragranular misorientation rather than the dislocation entanglement at dislocation walls, which ought to be evaluated as dislocation hardening later. Therefore, we should take coarser grains surrounded by HAGBs into account while calculating d. From **Fig. 5**, the average grain size of CoCrNi alloy after RA treatment is 5.08 μm. As a consequence, the yield strength contributing from grain refinement is evaluated as 117.6 MPa.

The contribution of σ_{dis} can be estimated according to Taylor's hardening law [53]:

$$\sigma_{dis} = M \cdot \alpha \cdot G \cdot b \cdot \rho^{0.5} \quad (4)$$

where M, α, G, b, and ρ are the Taylor factor, empirical constant, shear modulus, Burgers vector, and dislocation density, respectively. For the CoCrNi alloy, the above parameters are M = 3.06 [43], α= 0.2 [54], G = 85 GPa [5], b = 0.253 nm [6]. In the refined hierarchical structure of CoCrNi alloys, the pre-existing high-density dislocation formed in SLM and maintained during cold rolling and annealing process will substantially contribute to dislocation hardening. According to the strengthening analysis of SLM-built CrMnFeCoNi alloys carried out by Zhu et al. [39] and Kocks [53], the dislocation density term is directly related to the mean cell size λ (128 nm, based on TEM results):

$$\sqrt{\rho} = c / \lambda \quad (5)$$

where c is a constant with $\alpha c \approx 1$ [37,53]. Consequently, the contribution of dislocation density is about 514.1 MPa. The estimated yield strength is ~ 849.7 MPa, which is lower than the measured yield strength of 1161.6 MPa. Therefore, the high yield strength of CoCrNi alloys should also originate from other factors.

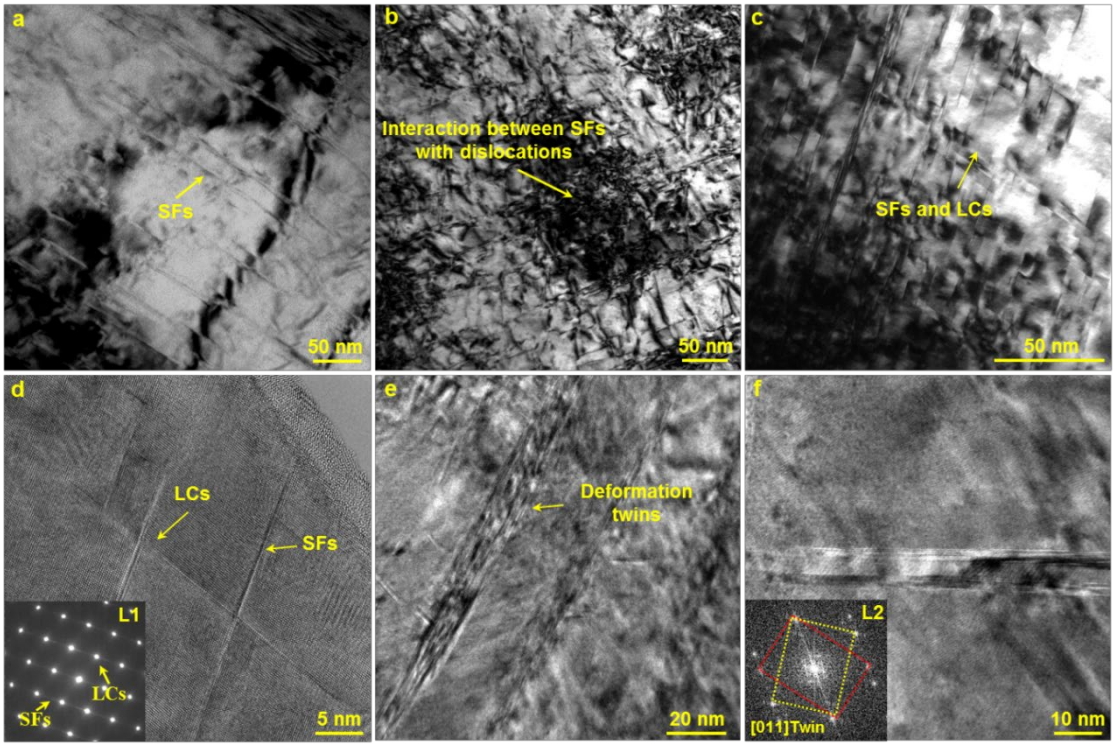

Figure 9. TEM micrographs after tensile testing of as-SLMed CoCrNi alloys with RA treatment showing (a) the formation of stacking faults; (b) the interaction between stacking faults and dislocations; (c) STEM image, (d) high-resolution TEM image and SAED (L1) showing the formation of Lomer-Cottrell locks; (e) TEM image, (f) high-resolution TEM image and SAED (L2) showing the formation of deformation twins.

Apart from the refined heterogeneous grain structures and the dislocations-formed equiaxed

and columnar sub-grains, we also observed other lattice defects that formed during tensile testing, as indicated in **Fig. 9**. High density of SFs nucleated and grew from the matrix, and the interaction between SFs and dislocations are observed in **Fig. 9a&9b**. **Fig. 9c&9d** show STEM image and high-resolution TEM image with SAED pattern. It is seen that the SFs also moved and intersected to form Lomer-Cottrell locks (LCs). With the high density of SFs and LCs produced within a band-like structure, the dislocation transmission was hindered by SFs and LCs on the conjugate plane. Moreover, the deformation twins with nano-size were characterized by TEM image (**Fig. 9e**), HR-TEM image and SAED pattern of L2 (**Fig. 9f**). Previous studies [54–56] have confirmed that slips were arrested at grain boundaries in the low SFE fcc alloys. With increasing the applied stress, the numbers of dislocations pileups decide the levels of the critical stress above which the occurrences of numerous slips transmit across the boundaries. In addition, residual deformation structures consisting of multiple kinds of lattice defects (such as deformation twins, stacking faults and LC locks and tangled high-density dislocations) were also observed in the CrCoNi alloy after RA treatment. These can increase the heterogeneity of the annealed microstructure, further promoting strain partitioning and strain gradients among heterogeneous domains, and therefore contribute to additional strain hardening and strengthening.

Particularly, the SLMed CoCrNi alloys with RA treatment maintain a large fracture strain of 31.5%. We expect that the good ductility of this alloy was partially due to the formation of bimodal grain size distribution, as shown in **Fig. 5d&5e**. In such heterogeneous grain structures, the soft coarse grains (> 4 μm, 43.1%) and hard ultrafine grains (< 4 μm, 56.9%) are mixed together, leading to evident microstructural heterogeneities. During plastic deformation, soft large grains can deform plastically more easily than hard small grains, causing significant mechanical incompatibility and strain partitioning, and thus resulting in the occurrence of large strain gradient. In fact, design of heterogeneous microstructures has been extensively studied and confirmed as an effective strategy to overcome the strength-ductility trade-off [14,57–60]. For example, Wang et al. [57] have demonstrated that pure Cu with a bimodal distribution of grain sizes can deliver a good plasticity comparable to that of the conventional coarse-grained Cu; however, it still retains the high strength as ultrafine-grained Cu. This design strategy of architecting heterogeneous grain structure has also been employed in MEAs and HEAs to achieve superior strength and ductility [14,59,60]. For example, a partially recrystallized $Al_{0.1}$CoCrFeNi alloys with bimodal grain size can achieve the yield strength of 711 MPa and uniform elongation of 30.3%, displaying a surprisingly excellent strength–ductility combination in excess of that of the existing HEAs [59]. A three-level heterogeneous-grain-structured CrCoNi alloy with grain sizes spanning from the nanometer scale to the coarse

micrometer scale exhibits a yield strength beyond 1 GPa and uniform elongation of 22% [14,60]. Furthermore, a large amount of nano-sized annealing twins can be detected by STEM image of **Fig. 7e** and SAED pattern of **Fig. 7f**, which is characterised by the partially recrystallized mixture of heterogeneous grains and nano-sized annealing twin bundles. As shown in **Fig. 6b** and **Fig. 6f**, the fraction of HAGB decreases with RA treatment. Normally, HAGB mobility promoted the nucleation of the twins by dividing a migrated original grain boundary into an immovable twin, a movable twin, and a low angle grain boundary [61]. Generating annealing twin boundaries into materials can dramatically refine microstructures, and the twin spacing can even be considered as the equivalent grain size [62,63]. The nano-twin boundaries in the CrCoNi alloy can also provide adequate barriers to dislocation motion for strengthening. Meanwhile, they act as nucleation sites of dislocations to accommodate the aggregations, thereby enhancing the work hardening capability and the excellent tensile ductility of the CrCoNi alloy.

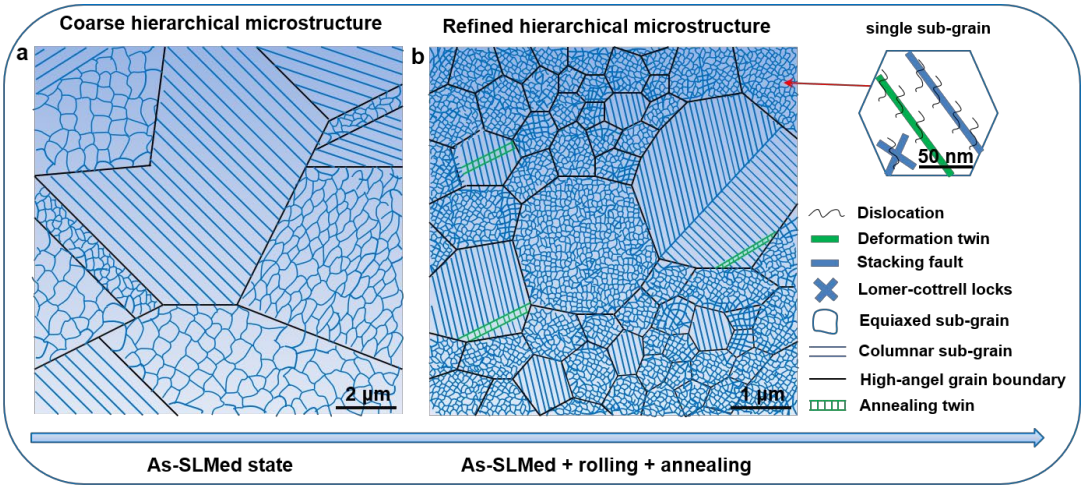

Figure 10. Schematic diagram showing (a) the coarse hierarchical microstructure of SLMed CoCrNi alloys and (b) the refined hierarchical microstructure of the SLMed CoCrNi alloy after RA treatment.

In summary, a representative diagram containing coarse and refined hierarchical microstructures in the studied CoCrNi alloy is schematically illustrated in **Fig. 10**. The typical dislocation-formed sub-grains in the coarse hierarchical microstructure delivered relatively good yield strength (~693.4 MPa), as shown in Fig. 10a. However, the coarse grains separated by HAGBs in the SLMed CoCrNi alloys weaken the grain boundary strengthening. With RA treatment, the enhanced mechanical properties (yield strength of 1161.6 MPa and the fracture strain of 31.5%) are attributed to three aspects: (*i*) the hierarchical microstructure that contain refined heterogeneous grain structure brought effective grain boundary strengthening effect; (*ii*) the refined dislocation-formed sub-grains distributed within heterogeneous grain structure delivered superior dislocation strengthening effect; (*iii*) It is probable that the strengthening

and hardening also originated from the capability of the lattice defects (i.e. the SFs, LCs, deformation twins and annealing twins) to accommodate dislocations, the annealing twins can also serve as a continuous source of ductility by providing pathways for the gliding or cross-slipping of dislocations, as shown in Fig. 10b.

5. Conclusions

(1) Regarding the CoCrNi medium entropy alloy, the selective laser melting with subsequent cold rolling and annealing is an effective technique to produce high-density lattice defects in the refined hierarchical microstructures.

(2) The SLMed CoCrNi alloy with RA treatment offers a remarkable synergistic trade-off in strengthen and ductility. The purely as-SLMed alloys can deliver the yield strength of 693.4 MPa, the UTS of 912.7MPa and the fracture strain of 54.4%. After RA treatment, the yield strength, UTS and fracture strain can reach 1161.6 MPa, 1390.8 MPa and 31.5%, respectively.

(3) With RA treatment, the refined hierarchical and heterogeneous grains (5.08 μm), high-density dislocation-formed sub-grains and lattice defects contribute to the improvement in strength. The heterogeneous structures in association with the annealing twins and lattice defects promote strain gradients among heterogeneous domains and thus lead to a superior fracture strain of 31.5%.

(4) The manufacturing technique using selective laser melting + rolling/annealing offers a new strategy in materials design for improving the mechanical properties of CoCrNi alloy.

Acknowledgments

Financial support from the National Key Research and Development Program of China (grant number 2020YFB0311300ZL) is greatly acknowledged. Financial support from National Natural Science Foundation of China (No. 52071343) is also greatly acknowledged.

References

[1] J.W. Yeh, S.K. Chen, S.J. Lin, J.Y. Gan, T.S. Chin, T.T. Shun, C.H. Tsau, S.Y. Chang, Adv. Eng. Mater. 6 (2004) 299–303.

[2] B. Cantor, I.T.H. Chang, P. Knight, A.J.B. Vincent, Mater. Sci. Eng. A 375–377 (2004) 213–218.

[3] J.Y. Wang, H.L. Yang, H. Huang, J.P. Zou, S. Ji, Z.L. Liu, Mater. Sci. Eng A 9 (2020) 139974.

[4] X. Lu, D. Wang, Z.M. Li, Y. Deng, A. Barnoush, Mater. Sci. Eng. A 762 (2019) 138114.

[5] J.Y. Wang, H.L. Yang, H. Huang, J.M. Ruan, S. Ji, J. Alloys. Compd. 798 (2019) 576–586.

[6] Y.L. Zhao, T. Yang, Y. Tong, J. Wang, J.H. Luan, Z.B. Jiao, D. Chen, Y. Yang, A. Hu, C.T.

Liu, J.J. Kai, Acta Mater. 138 (2017) 72–82.
[7] Z. Zhang, H. Sheng, Z. Wang, B. Gludovatz, Z. Zhang, E.P. George, Q. Yu, S.X. Mao, R.O. Ritchie, Nat. Commun. 8 (2017) 14390.
[8] G. Laplanche, A. Kostka, C. Reinhart, J. Hunfeld, G. Eggeler, E.P. George, Acta Mater. 128 (2017) 292–303.
[9] S. Zhao, G.M. Stocks, Y. Zhang, Acta Mater. 134 (2017) 334–345.
[10] J.B. Li, B. Gao, Y.T. Wang, X.H. Chen, Y.C. Xin, S. Tang, B. Liu, Y. Liu, M. Song, J. Alloys Compd. 792 (2019) 170–179.
[11] J.B. Seol, J.W. Bae, J.G. Kim, H. Sung, Z.M. Li, H.H. Lee, S.H. Shim, J.H. Jang, W.S. Ko, S.I. Hong, H.S. Kim, Acta Mater. 194 (2020) 366–377.
[12] J. Miao, C.E. Slone, T.M. Smith, C. Niu, H. Bei, M. Ghazisaeidi, G.M. Pharr, M.J. Mills, Acta Mater. 132 (2017) 35–48.
[13] C.E. Slone, S. Chakraborty, J. Miao, E.P. George, M.J. Mills, S.R. Niezgoda, Acta Mater. 158 (2018) 38–52.
[14] C.E. Slone, J. Miao, E.P. George, M.J. Mills, Acta Mater. 165 (2019) 496–507.
[15] J.Y. Wang, W.H. Li, H.L. Yang, H. Huang, S. Ji, J.M. Ruan, Z.L. Liu, Corro. Sci. 177 (2020) 108973.
[16] B. Gludovatz, A. Hohenwarter, K.V.S. Thurston, H.B. Bei, Z.G. Wu, E.P. George, R.O. Ritchie, Nat. Commun. 7 (2016) 10602–10609.
[17] J.S. Miao, C. Slone, S. Dasari, M. Ghazisaeidi, R. Banerjee, E.P. George, M.J. Mills, Acta Mater. 210 (2021) 116829.
[18] J.Y. Wang, H.L. Yang, J.M. Ruan, Y. Wang, S. Ji, J. Mater. Res. 34 (12) (2019) 1–11.
[19] I. Moravick, L. Gouvea, J. Cupera, I. Dlouhy, J. Alloys Compd. 5 (2018) 979–988.
[20] F. Otto, A. Dlouhý, Ch Somsen, H. Bei, G. Eggeler, E.P. George, Acta Mater. 61 (15) (2013) 5743–5755.
[21] R. SreeGanji, P. Sai Karthik, K. Bhanu Sankara Rao, K.V. Rajulapati, Acta Mater. 125 (2017) 58–68.
[22] X.Y. Li, K. Lu, Nat. Mater. 16 (2017) 700–701.
[23] H. Wu, G. Fan, Prog. Mater. Sci. 113 (2020) 100675.
[24] S. Yoshida, T. Bhattacharjee, Y. Bai, N. Tsuji, Scripta Mater. 134 (2017) 33–36.
[25] E.O. Hall, Proc. Phys. Soc. London B 64 (1951) 747.
[26] N.J. Petch, J. Iron Steel Inst. 174 (1653) 25.
[27] I. Moravcik, J. Cizek, Z. Kovacova, J. Nejezchlebova, M. Kitzmantel, E. Neubauer, I. Kubena, V. Hornik, I. Dlouhy, Mate. Sci. Eng. A 701 (2017) 370–380.
[28] H. Huang, J.Y. Wang, H.L. Yang, S. Ji, H.L. Yu, Z.L. Liu, Scripta Mater. 188 (2020) 216–

221.
[29] E.O. Olakanmi, R.F. Cochrane, K.W. Dalgarno, Prog. Mater. Sci. 74 (2015) 401–477.
[30] R.D. Li, M.B. Wang, Z.M. Li, P. Cao, T.C. Yuan, H.B. Zhu, Acta Mater. 193 (2020) 83–98.
[31] H.L. Yang, Y.Y. Zhang, J.Y. Wang, Z.L. Liu, C.H. Liu, S.X. Ji, J. Mater. Sci. Tech. 91 (2021) 215–223.
[32] H. Gong, K. Raf, H. Gu, G.D. Janaki Ram, T. Starr, B. Stucker, Mater. Des. 86 (2015) 545–554.
[33] W. Xu, M. Brandt, S. Sun, J. Elambasseril, Q. Liu, K. Latham, K. Xia, M. Qian, Acta Mater. 85 (2015) 74–84.
[34] D.D. Dong, C. Chang, H. Wang, X.C. Yan, W.Y. Ma, M. Liu, S.H. Deng, J. Gardan, R. Bolot, H.L. Liao, J. Mater. Sci. Tech. 73 (2021) 151–164.
[35] L. Liu, Q. Ding, Y. Zhong, J. Zou, J. Wu, Y.-L. Chiu, J. Li, Z. Zhang, Q. Yu, Z. Shen, Mater. Today. 21 (4) (2018) 354–361.
[36] D.Y. Deng, R.L. Peng, J. Moverare, Mater. Sci. Eng. A 21 (2020) 140072.
[37] X.Q. Wang, L.N. Carter, B. Pang, M.M. Attallah, M.H. Loretto, Acta Mater. 128 (2017) 87–95.
[38] J.B. Gao, Y.T. Jin, Y. Q. Fan, D. Xu, L. Meng, C. Wang, Y.P. Yu, D.L. Zhang, J. Mater. Sci. Tech. 102 (2022) 159–165.
[39] Z.G. Zhu, Q.B. Nguyen, F.L. Ng, X.H. An, X.Z. Liao, P.K. Liaw, S.M.L. Nai, J. Wei, Scripta Mater. 154 (2018) 20–24.
[40] B.L. Han, C.C. Zhang, K. Feng, Z.G. Li, X.C. Zhang, Y. Shen, X.D. Wang, H. Kokawa, R.F. Li, Z.Y. Wang, P.K. Chu, Mater. Sci. Eng. A 820 (2021) 141545.
[41] P.D. Niu, R.D. Li, K.F. Gan, T.C. Yuan, S.Y. Xie, C. Chao, Microstructure, Metall. Mater. Trans. A 52 (2021) 753–766.
[42] R.L. Ma, C.Q. Peng, Z.Y. Cai, R.C. Wang, Z.H. Zhou, X.G. Li, X.Y. Cao, Mater. Sci. Eng. A 775 (2020) 138975.
[43] T. Zhang, H.G. Li, H. Gong, Y.X. Wu, A.S. Ahmad, X. Chen, J. Alloys. Compds. 884 (2021) 161050.
[44] L. Lemarquis, P.F. Giroux, H. Mskrot, B. Barkia, O. Hercher, P. Castany, J. Mater. Res. Tech. 15 (2021) 4725–4736.
[45] J.Y. He, H. Wang, H.L. Huang, X.D. Xu, M.W. Chen, Y. Wu, X.J. Liu, T.G. Nieh, K. An, Z.P. Lu, Acta Mater.102 (2016) 187–196.
[46] R.B. Chang, W. Fang, H.Y. Yu, X. Bai, X. Zhang, B.X. Liu, F.X. Yin, Scipta Mater. 172 (2019) 144–148.

[47] Z. Tong, X. Ren, J. Jiao, W. Zhou, Y. Ren, Y. Ye, E.A. Larson, J. Gu, J. Alloy Compd. 785 (2019) 1144–1159.

[48] X.L. Ma, C.X. Huang, J. Moering, M. Ruppert, H.W. HÖppel, M. GÖken, J. Narayan, Y. Zhu, Acta Mater. 116 (2016) 43–52.

[49] S.C. Li, C.Y. Guo, L.L. Hao, Y.L. Kang, Y.G. An, Mater. Sci. Eng. A 759 (2019) 624–632.

[50] M. Zaiser, E.C. Aifantis, Scripta Mater. 48 (2) (2003) 133–139.

[51] Y.M. Wang, T. Voisin, J.T. McKeown, J. Ye, N.P. Calta, Z. Li, Z. Zeng, Y. Zhang, W. Chen, T.T. Roehling, R.T. Ott, M.K. Santala, P.J. Depond, M.J. Matthews, A. V. Hamza, T. Zhu, Nat. Mater. 17 (1) (2018) 63–71.

[52] N. Hansen, Scripta Mater. 51 (2004) 801–806.

[53] U.F. Kocks, H. Mecking, Prog. Mater. Sci. 48 (3) (2003) 171–273.

[54] M.D. Sangid, T. Ezaz, H. Sehitoglu, I.M. Robertson, Acta Mater. 59 (2011) 283–296.

[55] Y.L. Zhang, J.G. Li, X.G. Wang, Y.P. Lu, Y.Z. Zhou, X.F. Sun, J. Mater. Sci. Technol. 35 (2019) 902–906.

[56] J.H. Lee, T.B. Holland, A.K. Mukherjee, X.H. Zhang, H.Y. Wang, Sci. Rep. 3 (2013) 1061.

[57] Y.M. Wang, M. Chen, F. Zhou, E. Ma, Nature 419 (2002) 912.

[58] X. Wu, M. Yang, F. Yuan, G. Wu, Y. Wei, X. Huang, Y. Zhu, Proc. Natl. Acad. Sci. Unit. States Am. 112 (2015) 14501–14505.

[59] S.W. Wu, G. Wang, Q. Wang, Y.D. Jia, J. Yi, Q.J. Zhai, J.B. Liu, B.A. Sun, H.J. Chu, J. Shen, P.K. Liaw, C.T. Liu, T.Y. Zhang, Acta Mater. 165 (2019) 444–458.

[60] M. Yang, D. Yan, F. Yuan, P. Jiang, E. Ma, X. Wu, Proc. Natl. Acad. Sci. Unit. States Am. 115 (2018) 7224–7229.

[61] S. Mahajan, C.S. Pande, M.A. Imam, B.B. Rath, Acta Mater. 45 (1997) 2633–2638.

[62] A. Rohatgi, K.S. Vecchio, G.T. Gray, Metall. Mater. Trans. A 32 (1) (2001) 135–145.

[63] X.P. Chen, L.F. Li, H.F. Sun, L.X. Wang, Q. Liu, Mater. Sci. Eng. A 622 (2015)108–113.